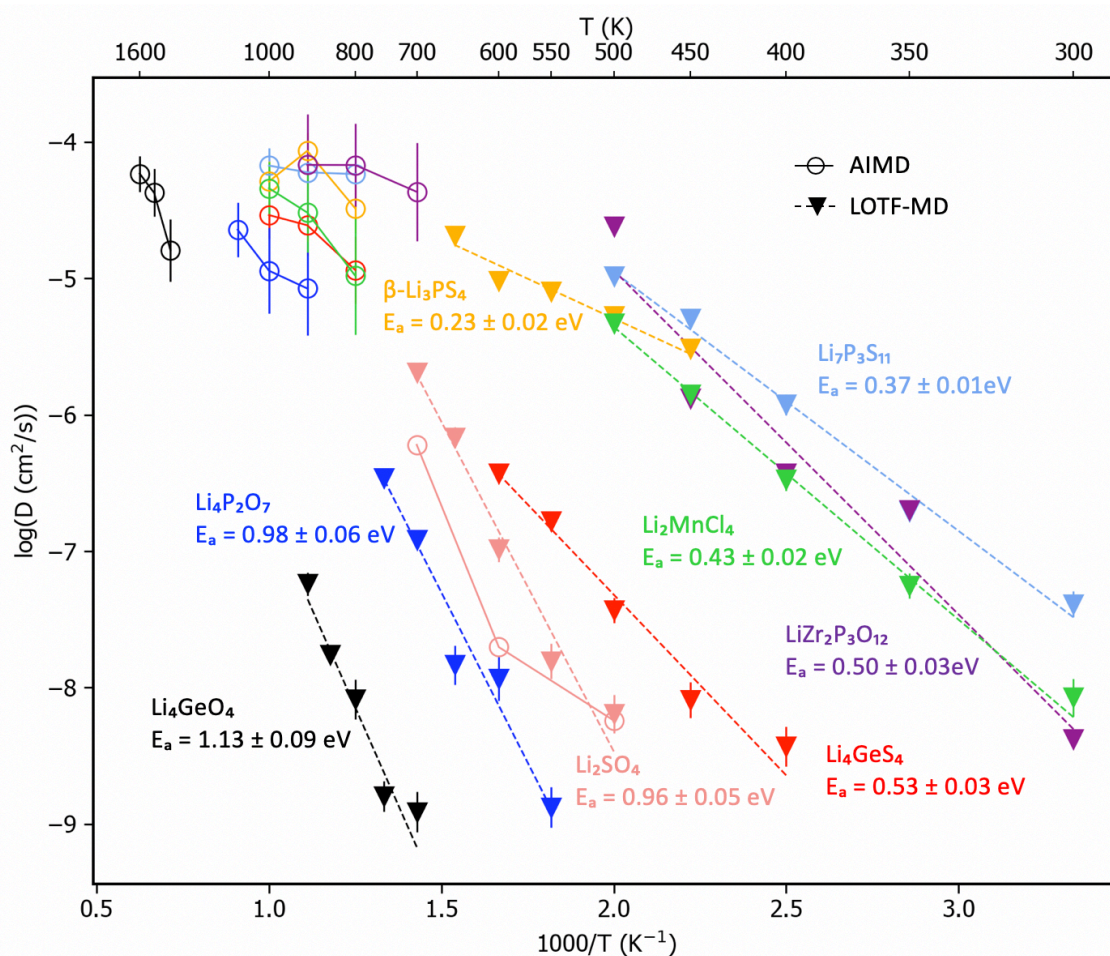# Lithium Ion Conduction in Cathode Coating Materials from On-the-Fly Machine Learning

Chuhong Wang[a], Koutarou Aoyagi[a,b], Pandu Wisesa[a], Tim Mueller[a,*]

[a]Department of Materials Science and Engineering, Johns Hopkins University

[b]Toyota Motor Corporation.

*Corresponding Author
Tim Mueller
Department of Materials Science and Engineering
Johns Hopkins University
3400 N. Charles St.
Baltimore, MD 21218 USA
(410)516-5779
tmueller@jhu.edu

ABSTRACT

The performance of solid state lithium ion batteries can be improved through the use of interfacial coating materials, but computationally identifying materials with sufficiently high lithium-ion conductivity can be challenging. Methods such as ab-initio molecular dynamics that work well for superionic conductors can be prohibitively expensive when used on materials that conduct lithium ions less well but are still suitable for use as interfacial coatings. We demonstrate a way to address this problem using machine-learned interatomic potentials models in the form of moment tensor potentials. To prevent the potentials from significantly deviating from density functional theory calculations we use molecular dynamics simulations coupled with on-the-fly machine learning. This approach increases the efficiency of the calculations by seven orders of magnitude compared to purely ab initio molecular dynamics, significantly reducing the uncertainty in calculated migration energies and improving agreement with experimentally-determined activation energies. Using this approach, we identify two particularly promising materials for use as coatings in batteries as well as several others that are candidates for doping-enhanced ionic conduction.

1. INTRODUCTION

Lithium-ion batteries have become the dominant energy storage devices for portable electronics and electric vehicles. These batteries convert Li chemical potential differences into electric current by shuttling lithium ions between two electrodes. Due to the low atomic weight and highly electropositive nature of lithium, lithium-ion batteries can achieve high energy density, high rate capability, and long cycle life.[1] Compared with a liquid electrolyte, the use of solid-state electrolytes has emerged as an appealing alternative that has the potential to accommodate higher-voltage cathode materials and a metallic lithium anode.[2,3]

Considerable research efforts have focused on identifying solid-state electrolytes with high ionic conductivity. The lithium-ion conductivities of several families of electrolytes, such as $Li_{10}GeP_2S_{12}$ and $Li_7P_3S_{11}$, are approaching that of liquid electrolytes at 10^{-2} S/cm.[4] Despite the high bulk conductivity of battery components, the actual rate capability of all-solid-state batteries is generally lower than estimated, especially at high states of charge or at high temperatures. The degradation of battery performance is typically attributed to increased impedance at the interface between electrodes and the electrolyte.[2,5-9] Studies suggest that the two main causes of high interfacial resistance are poor contact between the electrode and electrolyte and formation of undesired interphases.[6,10,11] The prevailing issue of interface reactivity originates from abrupt electrochemical potential changes at the electrode-electrolyte interface,[8,12-15] which can be addressed by putting a protective coating layer between the incompatible materials.[11,16-23] Materials with desirable chemical and electrochemical stability against both the electrode and the electrolyte can function as an interlayer that eliminates any unanticipated reactions and enhances the cyclability of the battery.

Previous progress on identification of protective coating materials was achieved primarily by experimental trial and error. Typical protective coating materials between the cathode and sulfide-

based solid electrolytes include $LiNbO_3$,[24, 25] Li_2SiO_3,[26] $Li_4Ti_5O_{12}$,[18] $Li_2O\text{-}ZrO_2$,[27] $LiTaO_3$[28] and Li_3PO_4.[16] It has also been reported that garnet oxide electrolytes coated with Li_3BO_3[29], Li_2CO_3 and their mixtures[30] exhibit improved cycle life over non-coated systems. Theoretical predictions of cathode / electrolyte interfacial products and protective coatings are in good agreement with experimental observations.[12, 15, 31] With reliable ab initio databases such as those provided by the Materials Project[32] and Open Quantum Materials Database[33] (OQMD), thermodynamic analysis of phase equilibria can be performed in a high-throughput fashion. Snydacker et al.[34] have performed a high-throughput screening to identify coating materials that are predicted to form stable interfaces with metallic (Na, Li, and Mg) anodes. Aykol et al.[31] screened the OQMD database for coatings that stabilize the interface between the cathodes and liquid electrolytes by considering their thermodynamic stability, electrochemical stability, and hydrofluoric acid reactivity. Recently, Xiao et al.[35] demonstrated a high-throughput screening scheme for coating materials based on similar criteria with an additional requirement on chemical stability with the sulfide electrolyte and the oxide cathode.

One of the greatest obstacles to the integration of these identified compounds as functional interface coatings is the inherently inhibited Li^+ conduction in many candidate coating materials, which compromises the battery's rate capability. The chance that a randomly chosen material forms stable interfaces and conducts Li^+ quickly is unfortunately small. Fast lithium ion conductors have been found in sulfide compounds, but they are susceptible to be oxidized by the cathodes. This is consistent with the fact that the identified stable protective coatings are made up of oxides, halides, nitrides but few sulfides. Across four decades of materials discovery for solid electrolytes, only a handful of oxide-based structure families with liquid-level Li conduction ($>10^{-2}$ S/cm) at room temperature have been identified.[36] This slow discovery in oxide-based superionic conductors indicates the scarcity of ultra-fast ionic conductors in this category. Stoichiometric oxides generally possess Li^+ conductivity lower than 10^{-6} S/cm at ambient temperature,[37] while ionic conductivity of chlorides and fluorides have been studied less.

In solid-state batteries, the thickness of the electrolyte is typically thousands of times larger than that of a coating layer between the electrode and electrolyte.[38] Lithium diffusion paths in interface coatings can be further shortened to the angstrom scale with state-of-the-art fabrication techniques.[39] Thus the requirement of high ionic conductivity for a coating layer is relaxed compared with the solid electrolyte. Assuming the time spent to pass through the surface coating can be approximated as the time frame for Li^+ transfer through micrometer-thick superionic conductor, materials with ionic conductivity of 10^{-6}-10^{-8} S/cm may be qualified to be integrated as nanometer-scale coatings without significantly affecting battery charge and discharge rates. Protective coating materials with moderate ionic conductivity could potentially strike a balance between long-term cyclability and high rate capability. In contrast to the pursuit of superionic conductors for solid electrolytes, a primary goal in coating design is to identify materials that exhibit a fast-to-medium Li^+ diffusion rate while maintaining chemical stability against both the solid electrolyte and the cathode.

Despite the critical role of viable Li^+ conduction in coating functionality, it is uncommon to find it as a search criterion in computational screening of coating materials. The main challenge lies in the high cost of accurate prediction of lithium ion conductivity. Current computational approaches for ionic conductivity evaluation include the climbing image nudged elastic band method,[40, 41] molecular dynamics simulations, and several ionic conductivity descriptors such as those based on lattice dynamics[42] or the bond-valance model.[43] The nudged elastic band method is frequently used to determine the energy of the transition state along the minimum energy path. Prior knowledge of the diffusion pathway in the structure is essential to initialize nudged elastic band calculations, which critically affects the accuracy of the calculated migration energy. (Throughout this manuscript we will refer to the calculated activation energy for lithium ion migration as the "migration energy".) The prior guess of the diffusion mechanism is challenging when searching for novel materials for which Li^+ conduction has not been characterized, especially in systems where Li^+ diffusion occurs via highly correlated motion as opposed to simple lithium ion hops into vacant sites. Possibilities of other diffusion mechanisms are often overlooked with this calculation method. Molecular dynamics (MD) has several advantages for computing Li^+ conductivity as well as for direct observation of hopping events. Molecular dynamics explores state space and identifies the states and mechanisms that are most conducive to high ionic conductivity. Due to the lack of well-developed interatomic potentials over a wide chemical space, ab initio molecular dynamics (AIMD) has been widely used for exploring new ionic conductors. However, as this method is computationally demanding, the time scale of a simulation is typically limited to tens to hundreds of picoseconds. Since cation migration becomes exponentially slower as the migration energy increases, AIMD is only suitable for the determination of conductivity at room temperature when the migration energy is lower than about 0.2 eV, and even for a material with such a low migration energy there can be significant error in the predicted diffusivity.[44] Modeling materials with higher migration energies requires simulations at higher temperatures which can only be used to extrapolate room temperature conductivity if no phase transformation take place between room temperature and the temperatures at which AIMD simulations are run. This presents a problem for the types of materials with moderate Li^+ conductivity that may be used as coating materials, as it may not be possible to calculate accurate diffusion rates at low temperatures because insufficient statistical data can be captured within AIMD simulation time scales at reasonable computational cost.[44]

To expand the timescale of AIMD and retain a similar level of accuracy, machine-learned interatomic potentials parameterized by ab initio data have been employed to optimize the efficiency-versus-accuracy tradeoff.[45-50] Such interatomic potential models are capable of simulating dynamics orders of magnitude faster than DFT and scale linearly with system size. The computational cost of such models is typically dominated by the cost of generating the data used to train them. To minimize the amount of data required to train a potential model while reducing the likelihood that the model has large prediction errors, active learning methods can be used to automatically decide whether a configuration encountered during molecular dynamics can be treated reliably by

a machine learning model or if the model needs to be retrained with more data points.[51, 52] This strategy, sometimes referred to as "learning on the fly" (LOTF), preserves the accuracy of machine learning potentials and prevents highly unphysical atomic dynamics.

We present a workflow for calculating lithium ion diffusivities based on a learning-on-the-fly scheme with moment tensor potentials (MTP), a recently-developed machine-learned interatomic potential model.[45] As a statistical method, the accuracy of diffusivity values calculated from molecular dynamics trajectories relies on the amount of observed diffusion events. As the LOTF/MTP approach reduces the computing time for each time step by about 7 orders of magnitude relative to DFT, we are able to extend the length of MD simulations to hundreds of nanoseconds with accuracy in the predicted energies that is comparable to DFT. Consequently, we are able to make accurate numerical predictions of low-to-medium migration energies (up to about 0.8 eV) for lithium ion diffusion and identify new candidate coating materials. Thus this framework enables an efficient and automated search for viable ionic conductors as protective coating materials.

2. METHODS

2.1 Ab initio molecular dynamics

AIMD simulations were performed using the PBE GGA functional[53] and projector augmented wave[54] potentials as listed in the Supplementary Information (SI). In line with previous reports,[55, 56] the calculation parameters were selected to balance accuracy versus computational cost. We used a plane wave energy cut-off of 400 eV and a minimal Γ-centered $1 \times 1 \times 1$ k-point mesh. Computations are performed with spin polarization and with magnetic ions initialized in a high-spin ferromagnetic state for materials containing transition metal atom(s). Non-spin-polarized calculations were performed otherwise. A time step of 2 fs was adopted. The supercell sizes were constructed to ensure there were at least 9 Å between neighboring images[55] to avoid periodic boundary effects. The lattice parameter is fixed at that of the cell fully relaxed at 0 K.

In each AIMD run, the material is firstly equilibrated at the target temperature for 2 ps and then a 13 ps dynamic trajectory is produced. For each material, AIMD is initially performed at 1600 K. If the averaged mean-square-displacement of non-lithium species exceeds 3 Å^2, partial melting is considered to have occurred and the temperature is discarded. The simulation temperature is decremented by 100 K and the process is repeated until we collect data points at three different temperatures for each benchmark material.

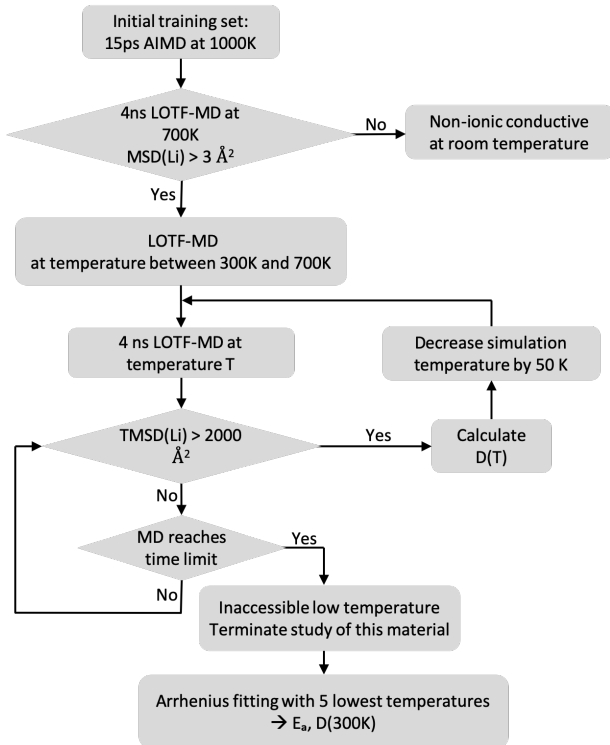## 2.2 Ionic conductors screening with learning on-the-fly MD

Initial training set:
15ps AIMD at 1000K

4ns LOTF-MD at
700K
MSD(Li) > 3 Å^2

No → Non-ionic conductive at room temperature

Yes

LOTF-MD
at temperature between 300K and 700K

4 ns LOTF-MD at temperature T

Decrease simulation temperature by 50 K

TMSD(Li) > 2000 Å^2 — Yes → Calculate D(T)

No

MD reaches time limit — Yes

No

Inaccessible low temperature
Terminate study of this material

Arrhenius fitting with 5 lowest temperatures
→ E$_a$, D(300K)

Figure 1. Flowchart of the LOTF-MD ionic conductor screening process.

To enable the automated screening of materials for lithium-ion conductivity, we developed a standardized workflow that can be applied to any crystalline material that contains lithium. The ionic conductor screening process is illustrated by the flowchart in Figure 1. For all moment tensor potentials we set the size of the polynomial basis using lev$_{max}$ = 10, where lev$_{max}$ is related to the maximum polynomial degree and defined in reference 57. The cut-off radius for the local atomic environment was set as 5 Å. The MTP models were trained on both DFT-calculated energies and DFT-calculated forces, with the forces given ten times the weight of the energies. All potentials were pre-trained by DFT data generated in AIMD simulations before being used in on-the-fly molecular dynamics simulations.

MTP molecular dynamics were run in LAMMPS.[58] The interface between moment tensor potential molecular dynamics and DFT geometry optimization was carried out by the Machine Learning of Interatomic Potentials (MLIP) software package.[59] During the dynamic evolution of the structure, MTP re-training is conditionally activated by the occurrence of an "unlabeled" configuration as determined by the D-optimality criterion,[60] corresponding to the *extrapolation grade*[59] parameter coded in MLIP. The maximal allowed extrapolation grade is defined as the *selection threshold*, the value of which can be specified by the user. It has been shown that a selection threshold value between 2 and 11 is a good choice for efficiency-versus-accuracy performance.[59] The molecular dynamics simulation is terminated once the extrapolation grade exceeds the selection threshold, which we set to 10. Then structures with extrapolation grade over 1.5 are selected from the molecular dynamics trajectory to be added to the DFT training set. DFT calculations on these structures are performed in VASP with DFT input parameters consistent with the initial AIMD simulation. The DFT-calculated structures are added to the training set, the MTP is retrained, and the molecular dynamics run is restarted with the new potential. By sampling the configurational space in this way, MTP eventually becomes sufficiently well-informed of the complete energy landscape that it needs no additional training data to complete the molecular dynamics simulation with sufficient accuracy.

For each structure the initial dataset used to train the MTP consists of 15 ps (2 fs per time step) of an AIMD simulation at 1000 K as described in 2.1. We chose a temperature for the initial training sets higher than the temperature range of interest for diffusivity to increase the likelihood that we adequately sample the space of structures likely to be encountered at lower temperatures, as suggested by Novoselov et al.[61] We chose a temperature lower than that of the initial temperature for AIMD simulations (1600 K) to reduce the risk of an unwanted phase transition from the room-temperature structure (including melting).

In the MLIP learning-on-the-fly implementation, the MTP molecular dynamics simulation is restarted from its initial state every time DFT is requested. In addition, each DFT calculation on a structure during the LOTF stage starts from scratch, which requires significantly more computing time than in an AIMD simulation where the charge density for a structure is initialized based on previous steps. For these reasons, a desirable initial training set should contain sufficient data so that re-training is rarely prompted during the MTP molecular dynamics run. To estimate the proper timescale of the 1000 K AIMD simulations used to generate the initial dataset, we tested different lengths of the initial molecular dynamics run. In general, we found that with MTP trained on 7500 configurations, the length of the LOTF-MD trajectories could typically reach the order of nanosecond before the first DFT request is activated.

In each MTP molecular dynamics run, we firstly equilibrate the structure at the target temperature for 20 ps. The molecular dynamics simulation is terminated when at least 4 ns of statistics have been gathered and the total mean squared displacement (TMSD) of Li^+ exceeds 2000 $Å^2$. Based on benchmarking work done by He et al,[44] simulations in which the TMSD reaches 2000 $Å^2$ are estimated to be sufficient to converge predicted diffusivity values with a standard deviation of about 27% of the diffusivity. At each temperature, the maximum length of molecular dynamics is set as 200 ns. Within this time scale and assuming 20 lithium atoms per simulation cell (which is typical for the compounds studied in this work), we estimate we can calculate diffusivities as low as about 2×10^{-9} cm^2/s with an estimated standard deviation less than 50% of the diffusivity (the derivation is shown in Supplementary Information S3). To identify the onset of possible melting, we also calculate the mean squared displacement of species other than lithium. We determine melting occurred if the mean squared displacement of non-lithium species exceeds 3 $Å^2$.

The initial temperature for our LOTF-MD simulations is 700 K. Li^+ hopping observed at 700K for 4 ns is used as the first filter to rule out unlikely room temperature Li^+ conductors. Using a typical hopping distance of 3 Å between neighboring Li sites and an activation energy of 0.5 eV, we estimate that the room-temperature diffusivity would be 6×10^{-13} cm^2/sec or lower if no Li diffusion is observed in 4 ns at 700 K (see the Supplementary Information S4 for derivation). For structures passing the first filter, the molecular dynamics production time, during which statistics are gathered, ranges from a minimum of 4 ns to a maximum of 200 ns depending on the Li^+ mobility in the structure. The use of a minimum simulation time is to improve statistical accuracy as well as the reliability of the moment tensor potential that is trained on the fly. Diffusivity data points are collected at temperatures decremented by 50 K until the diffusivity is so low that the

total mean squared displacement does not reach 2000 Å^2 within 200 ns. The lowest five qualifying temperatures are used to fit the Arrhenius relationship. The increase in the number of samples relative to AIMD is made possible by the dramatically improved speed of LOTF-MD.

2.3 Arrhenius parameters fitting and statistical uncertainties estimation

The tracer diffusion coefficient (D_{tr}) of the diffusing species is given by the slope of the mean squared displacement averaged over all diffusing atoms:

$$D_{tr} = \lim_{t \to \infty} \frac{\frac{1}{N} \sum_{i=1}^{N} \left\langle \left\| \mathbf{r_i}(t) - \mathbf{r_i}(0) \right\|^2 \right\rangle}{6t} \tag{1}$$

where $\mathbf{r_i}(t)$ is the position of the ith particle after time t, N is the number of lithium ions, and the constant 6 is used for three-dimensional diffusion. We denote the estimated tracer diffusivity at temperature T as $D(T)$. Following the Arrhenius relationship,

$$D(T) = D(\infty) e^{-\frac{E_a}{k_B T}} \tag{2}$$

the activation energy E_a, can be calculated from a linear fit of $\log(D(T))$ to $\frac{1}{k_B T}$, where k_B is Boltzmann's constant. Since the probability of ionic hopping decays exponentially at lower temperature, the calculated diffusivity at low temperatures may have a higher statistical uncertainty, especially from simulations terminated by the time limit instead of the TMSD criterion. Thus the variance of the independent variable D should be taken into account when fitting the Arrhenius equation for a statistically meaningful estimation of E_a. We estimated the variance of the diffusivity of lithium ions using the equation reported by He et al.[44] and propagated to the variance of $\log(D)$ using equation (7) in Supplementary Information S5. These variances were then used in a weighted least squares regression to estimate E_a. Details of the weighted least square regression are provided in Supplementary Information S5.

Using the Nernst−Einstein relation, assuming that the Haven ratio is equal to one,[62] the room temperature conductivity (σ) can be approximated by[63]

$$\sigma_{300K} = \frac{ne^2 z^2}{k_B T} D_{300K} \tag{3}$$

where n is the volume density of the diffusing species, e is the unit electron charge, z is the charge of the ionic conductor (here 1 for Li$^+$), and D_{300K} is the extrapolated room-temperature tracer diffusivity.

2.4 LOTF-MD diffusion study of structures that contain vacancies

In addition to the diffusion study on pristine stoichiometric structures, we studied vacancy-mediated diffusion by removing one lithium ion from the simulation supercell. In the *ab initio* training set, a background charge is applied to the system to maintain the oxidation states of the remaining atoms in the material upon cation removal. We note that the charge of the lithium vacancy may in practice be offset by other defects, which for simplicity we do not consider here. As the supercell size is held constant, any energy shift due to interactions between periodic charges and the chemical potential of the electrons is not expected to affect lithium diffusion dynamics. Following the same LOTF-MD workflow (section 2.2), MTP is trained on-the-fly by the DFT-calculated configurations containing one charged vacancy per supercell.

3. RESULTS AND DISCUSSION

3.1 LOTF-MD performance benchmark

To assess the efficiency and accuracy of the LOTF-MD framework, we selected eight lithium-containing crystalline structures including oxides, sulfides and chlorides for which experimentally measured activation energies have been reported. Among these benchmark materials, the activation energies measured by electrochemical impedance spectroscopy range from 0.2 eV to 1.2 eV. Moment tensor potentials were developed for each material, with root-mean-square fitting errors for energies and forces of 5 meV/atom and 0.24 eV/Å respectively for the configurations used to pre-train the potentials.

Over the 8 benchmark materials, the mean absolute error for calculated migration energies relative to experimental activation energies is 0.13 eV when the migration energy is calculated by LOTF-MD and 0.32 eV when it is calculated by AIMD (Table 1). This improvement is primarily due to two effects. The first is that the quality of linear correlation between log(D) vs. 1/T is greatly improved by LOTF-MD (average $R^2 = 0.97$) as compared with AIMD (average $R^2 = 0.82$), especially for structures with intermediate-to-high migration energies (Figure 2). Statistically, improved linearity of the Arrhenius plots mainly results from the reduced statistical uncertainty in each diffusivity data point as a direct consequence of more ionic hops in LOTF-MD simulations.[44] The statistical uncertainty in predicted migration energies is similarly reduced (Table 1).

The second reason for the improved accuracy is that the LOTF-MD simulations are better able to model room-temperature phases, as the simulations can be run at lower temperatures. For AIMD simulations of Li_4GeS_4 and $LiZr_2P_3O_{12}$ there is relatively little deviation from the Arrhenius linear fit (Figure 2), but the extrapolated migration energies for these materials were underestimated by 0.2 – 0.4 eV compared with the experimental activation energies at room temperature (Table 1). For these materials the assumption of an identical diffusion mechanism over the extrapolation temperature range does not strictly apply. Li_4GeS_4 is known to melt at about 850 °C.[64] Although partial melting was not observed in the fixed unit cell during AIMD simulations, the structural

9

instability at high temperatures likely led to a lower calculated migration energy than observed at lower temperatures. Similarly, $LiZr_2P_3O_{12}$ is known to undergo several temperature-dependent phase transitions among different polymorphs with different conductivities.[65, 66]

Due to the stochastic nature of the MD simulation, the accuracy of information extracted from MD trajectories depends on the amount of observed diffusion events. The benchmarks on Li_4GeS_4 and $LiZr_2P_3O_{12}$ suggest that although running simulations at high temperature can improve the statistics by sampling more diffusion events, this comes at the cost of compromised accuracy in the extrapolated properties for materials in which the stable high-temperature and room-temperature structures differ significantly. The LOTF-MD simulations, including the cost of all training data generation, generated about 10^7 times as much data as AIMD simulations per CPU hour (Table 2). Thus LOTF-MD is able to collect statistics at moderate temperatures that reduce the risk of unwanted structural transitions. The use of LOTF-MD reduced the difference between calculated migration energies and experimental activation energies from 0.21 eV to 0.01 eV for Li_4GeS_4 and from 0.46 eV to 0.09 eV for $LiZr_2P_3O_{12}$.
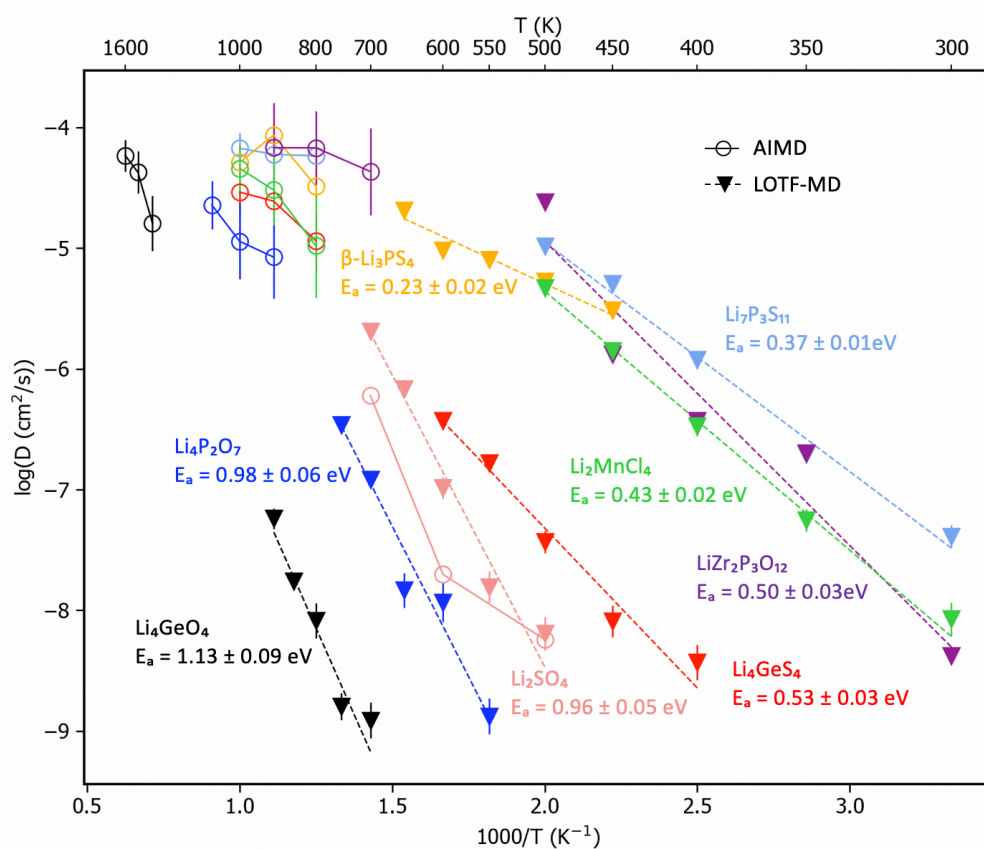

Figure 2. Diffusivities simulated by AIMD at high temperatures and by LOTF-MD at intermediate temperatures on the Arrhenius plot. The migration energies (eV) calculated by the weighted least square regression between log(D) vs. 1/T are shown next to the fitting dash line for LOTF-MD data set. The error bars indicate the magnitude of the estimated standard error of log(D).

Table 1. Experimental activation energies and calculated migration energies for 8 materials, listed with the estimated standard errors (stderr).

MP entry id	Composition	Experimental E_a (eV)	high-T AIMD				LOTF − MD			
			T (K)	R^2	$E_a \pm$ stderr (eV)	ΔE_a	T (K)	R^2	$E_a \pm$ stderr (eV)	ΔE_a
mp-10499	$LiZr_2P_3O_{12}$	0.59[65]	700 - 900	0.81	0.13±0.32	-0.46	300 − 500	0.94	0.50±0.01	-0.09
mp-30249	Li_4GeS_4	0.52[67]	800 - 1000	0.92	0.31±0.23	-0.21	400 − 600	0.97	0.53±0.03	-0.01
mp-4556	Li_2SO_4	1.2[68], 1.1[69]	500 - 700	0.88	0.41±0.52	-0.69	500 − 700	0.97	0.96±0.05	-0.19
mp-4558	Li_4GeO_4	0.82[70], 0.90[71]	1400 - 1600	0.94	1.16±0.57	0.30	700 − 900	0.95	1.14±0.09	0.28
mp-554577	$Li_4P_2O_7$	0.95[72]	900 - 1100	0.92	0.45±0.38	-0.5	550 − 750	0.96	0.99±0.06	0.04
mp-641703	$Li_7P_3S_{11}$	0.18[73]	800 - 1000	0.86	0.05±0.15	-0.13	300 − 500	0.99	0.38±0.01	0.2
mp-675083	Li_2MnCl_4	0.63[67]	800 - 1000	0.97	0.47±0.35	-0.16	300 − 500	0.99	0.43±0.02	-0.21
mp-985583	β-Li_3PS_4	0.16[74]	800 - 1000	0.27	0.13±0.19	-0.03	450 − 650	0.95	0.23±0.02	0.07

Table 2. Total computing time and MD production time for migration energy benchmark calculations

Method	Total CPU hour	MD time (ns)	production /cost (ns / CPU hour)
AIMD	23291	3.75×10^{-4}	1.61×10^{-8}
LOTF - MD	7186	1388	1.88×10^{-1}

3.2 Computational search for coating materials

We search for coating materials that are likely to be thermodynamically stable, as determined by their existence on the 0 K convex hull in the Materials Project database. As materials with a high concentration of Li sites are likely to provide more potential pathways for Li-ion conductivity,[35] we considered only materials with more than 10% mole fraction Li in our search for coating materials. From this set of compounds we identified 1545 materials. During battery operation, the cathode can undergo a drastic change in lithium chemical potential, which affects the chemical environment of the surface coating. To maintain interface equilibrium against the cathode throughout the charge/discharge cycle, the coating layer adjacent to an active electrode material is required to endure high Li chemical potentials without decomposition. Since the voltage of fully charged cathode materials is on the order of 4 V relative to metallic Li,[75] we screened for coating materials with an electrochemical oxidation voltage limit of at least 4 V using the grand phase diagram developed by Ong, S et.al.[55] We do not set a limit on the reduction voltage, requiring only interfacial stability between the coating material and the electronically insulating electrolyte. Using the above criteria, we found 234 qualified compounds by screening all the lithium-containing inorganic crystalline materials in Materials Project database.

Table 3. Oxide-based cathode and sulfide-based solid electrolyte materials studied in the work, composition of cathodes is displayed in charged / discharged states

Cathode	Solid Electrolyte
$LiCoO_2$ / $LiCo_2O_4$	$Li_7P_3S_{12}$
$LiFePO_4$ / $FePO_4$	$Li_{10}GeP_2S_{12}$
$LiMn_2O_4$ / MnO_2	$Li_{10}SnP_2S_{12}$
$Li(MnNiCo)_{1/3}O_2$ / $Li_{1/3}(MnNiCo)_{1/3}O_2$	$Li_{10}SiP_2S_{12}$
$LiMn_{1.5}Ni_{0.5}O_2$ / $Mn_{1.5}Ni_{0.5}O_2$	Li_6PS_5Br
	Li_6PS_5Cl

To avoid unwanted reactions at the interface, the protective coating material should also form thermodynamically stable interfaces with both the cathode and the solid electrolyte. In this work, we consider the five leading cathode materials and six solid electrolytes listed in Table 3. We specifically focused on the sulfide-based electrolyte materials because of their excellent ionic conductivity and mechanical compliance but high reaction susceptibility to reactions with oxide cathodes. A suitable cathode coating layer could significantly improve the performance of sulfide electrolyte batteries. Using the reactivity energy calculation method developed by Xiao et.al,[35] we identified 181 candidate cathode coatings showing no reactivity with at least one of the five cathode materials in both lithiated and delithiated phases. Of these 181 materials, 19 were determined to have no interfacial reaction energy with at least one of the sulfide electrolytes and were further investigated for ionic conductivity.

We applied the LOTF-MD workflow to calculate the lithium ion conductivity the 19 candidate coating materials. 14 materials exhibited mean squared displacements smaller than 9 $Å^2$ in 4 ns MD at 700 K. They were determined to be unlikely to conduct Li^+ at reasonable rates at room temperature and were removed from the screen. The remaining five candidate materials were LiCl, $Li_2B_3O_4F_3$, $Li_2B_6O_9F_2$, $Li_3B_7O_{12}$ and $Li_3Sc_2(PO_4)_3$. Li^+ conduction in $Li_2B_3O_4F_3$ notably slowed down as the temperature decreased from 700 K to 650 K, with a total mean squared displacement of only 1503 $Å^2$ after 200 ns. Thus it is unlikely that $Li_2B_3O_4F_3$ conducts lithium ions at a sufficiently high rate at room temperature. With ionic conduction studied at decremented temperatures following the LOTF-MD workflow, we were able to determine the migration energies for LiCl (1.11 ± 0.13 eV), $Li_3Sc_2(PO_4)_3$ (0.64 ± 0.04 eV), $Li_2B_6O_9F_2$ (0.79 ± 0.10 eV) and $Li_3B_7O_{12}$ (0.56 ± 0.05 eV). (Throughout this paper the values following the $\pm$ symbol for calculated migration energies represent the estimated standard error.) The migration energies and the extrapolated room temperature lithium ion conductivities are listed in Table 3, along with any available experimental values for reference.

LiCl has been shown to be a poor Li conductor[76] at room temperature with an experimental activation energy of 0.83 eV.[77] This activation energy is below our calculated migration energy by about 0.28 eV, which is consistent with the magnitude of ΔE_a for materials with similarly high activation energies in our benchmark set. The relatively large difference is accompanied by a relatively large uncertainty (± 0.13 eV) in the calculated value, as the number of diffusion events that can be sampled decreases exponentially

12

with migration energy. However materials with such high activation energies are unlikely to be good candidates for as coating materials; both the calculated migration energy and experimental activation energy indicate that if LiCl were to be used as a coating material it would likely be rate-limiting.

For $Li_3Sc_2(PO_4)_3$, we observed a slope change at 540 K on the Arrhenius plot (Figure 3), which indicates a phase transition. There is a reported superionic phase transition from a monoclinic (α-phase) to an orthorhombic (γ-phase) accompanied by an abrupt conductivity jump in the vicinity of 500 K.[78] We do not directly observe this phase transition due to our use of the NVT ensemble with a fixed lattice, but the discontinuity we observe at 540 K may be due to a related transition within the constraints of the lattice. The calculated low-temperature activation energy, 0.62 eV, is in good agreement with the experimentally-determined value of 0.68 eV for the low-temperature phase, and well above the activation energy of the high-temperature phase. This example is another demonstration of the importance of moderate simulation temperatures for accurate predictions. $Li_3Sc_2(PO_4)_3$ has been previously identified as a lithium ion conducting material from computational screening but the migration energy was underestimated by 0.35 eV due to the high temperature extrapolation.[79]
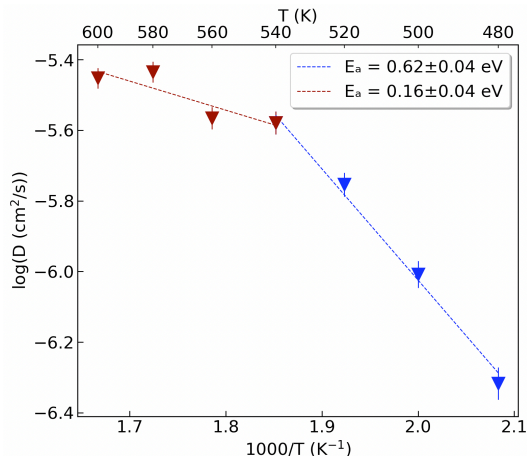

Figure 3. Calculated Arrhenius plot of $Li_3Sc_2(PO_4)_3$ with LOTF-MD. The error bars indicate the magnitude of the estimated standard error of log(D).

The remaining two candidates are the lithium borates $Li_2B_6O_9F_2$ and $Li_3B_7O_{12}$, the Arrhenius plots of which are shown in Figure 4. Lithium borates have been recognized for their excellent interfacial stability,[35] but ionic conductors in this category have rarely been identified.[80] The activation energy of lithium ion diffusion in $Li_2B_6O_9F_2$ has been experimentally determined to be 0.92 eV by heating the sample up to 623 K.[81] Using LOTF-MD, we calculated diffusivities from molecular dynamics simulations at temperatures as low as 570 K. The migration energy in $Li_2B_6O_9F_2$ calculated in the range of 570 K – 670 K is 0.79 ± 0.10 eV, which is 0.13 eV lower than the experimental activation energy. To our knowledge, $Li_3B_7O_{12}$, which is predicted to have excellent interfacial stability, has not been characterized in terms of Li^+ conduction. Our calculations predict that it has an intermediate migration energy 0.56 ± 0.05 eV and an estimated room-temperature conductivity of 9.95×10^{-8} S/cm.
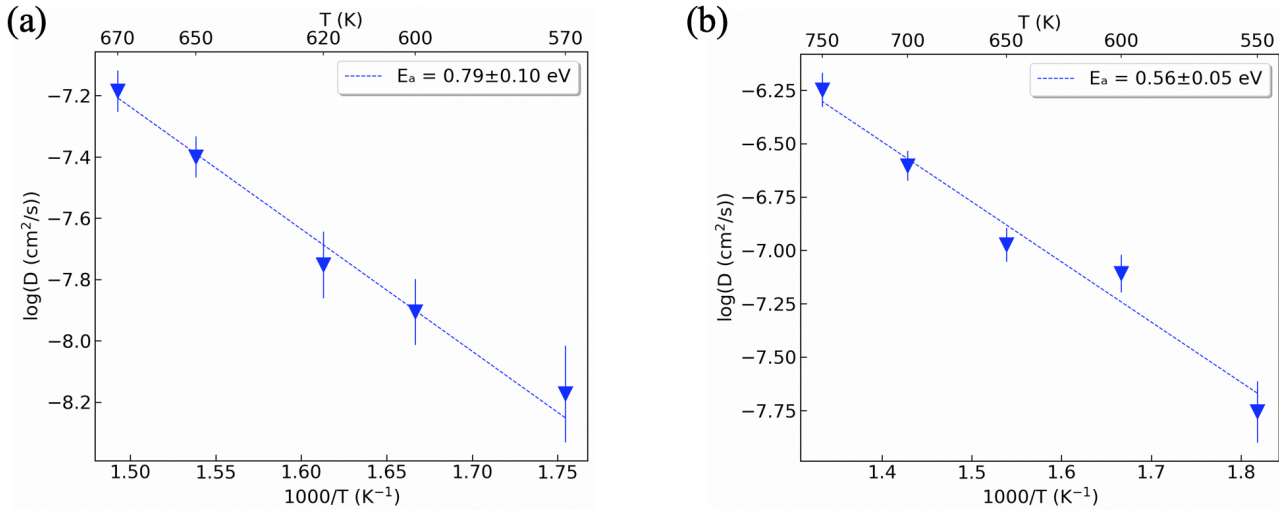
Figure 4. Calculated Arrhenius plot of (a) $Li_2B_6O_9F_2$ (b) $Li_3B_7O_{12}$ with LOTF-MD. The error bars indicate the magnitude of the estimated standard error of log(D).

The room temperature conductivities of $Li_3Sc_2(PO_4)_3$ and $Li_3B_7O_{12}$ potentially satisfy the rate criterion for a nanometer thick coating interlayer. They are promising coating candidates with reasonably high predicted Li^+ mobility and high predicted chemical/electrochemical stability.[35] $Li_3Sc_2(PO_4)_3$ is predicted to form a stable coating layer between $Li_7P_3S_{11}$ and the cathodes $Li(MnNiCo)_{1/3}O_2$ or $LiFePO_4$. $Li_2B_6O_9F_2$ is predicted to stabilize the interface between $Li_7P_3S_{11}$ and cathodes $Li(MnNiCo)_{1/3}O_2$, $LiFePO_4$ or $Li_2Mn_3NiO_8$ without largely compromising the battery efficiency. $Li_3B_7O_{12}$ is predicted to be stable against all six solid electrolytes listed in Table 3 cathodes $LiCoO_2$, $LiFePO_4$, and $Li(MnNiCo)_{1/3}O_2$.

3.3 Vacancy-mediated lithium-ion conduction

We have so far considered diffusion in defect-free materials, but lithium-ion conductivity may be higher through a vacancy-mediated mechanism. Through this mechanism, the migration energy is essentially the maximum activation energy for Li^+ hopping from one lattice site to an adjacent vacant site along the diffusion path. Using the approach described in section 2.3, we have calculated the migration energies for vacancy-mediated diffusion for the eight different benchmark materials using LOTF-MD (Table 5). As an experimental point of comparison, the activation energy for vacancy-mediated diffusion has been measured in doped Li_4GeO_4.[82] The experimentally-measured activation energy of 0.5 eV is in excellent agreement with the LOTF-MD prediction of 0.54 eV.

The activation energy for diffusion via a vacancy-mediated diffusion mechanism with intrinsic vacancies is the sum of the migration energy and the formation energy for a vacancy. Thus the difference between the experimentally-determined activation energy and the calculated migration energy for vacancy-mediated diffusion provides an estimate of the vacancy formation energy that would be required for vacancy-mediated diffusion to be the experimentally-observed diffusion mechanism in undoped materials. This difference is provided in the third column of Table 5. Computationally determining the intrinsic vacancy formation energies in each of these materials would require a full evaluation of the different combinations

14

of defects that could co-exist and is not attempted here. However the strong agreement between the experimentally-observed activation energies and the calculated migration energies for perfect crystals (Table 1) suggests that under the experimental conditions at which diffusion was measured, the dominant diffusion mechanism was not vacancy mediated.

Table 4. LOTF-MD simulated Li migration energies and room-temperature ionic conductivities for candidate coating materials

MP entry id	Composition	LOTF-MD $E_a \pm$ stderr (eV)	Experimental E_a (eV)	σ (300K) (S/cm)	Experimental Li^+ conductivity (S/cm)
mp-16828	$Li_3B_7O_{12}$	0.56 ± 0.05	--	9.95×10^{-8}	--
mp-6565	$Li_3Sc_2(PO_4)_3$	0.62 ± 0.04	$0.68^{[78]}, 0.76^{[83]}$	4.48×10^{-6}	$\sim 10^{-7}$ (360 K)
mp-1200209	$Li_2B_6O_9F_2$	0.79 ± 0.10	$0.92^{[81]}$	1.75×10^{-10}	2.2×10^{-10} (473 K)
mp-1185319	LiCl	1.11 ± 0.13	$0.83^{[77]}$	4.9×10^{-12}	$\sim 10^{-9}$ (300 K)
mp- 1196457	$Li_2B_3O_4F_3$,	--	$1.05^{[84]}$	--	1.6×10^{-9} (473 K)

We applied LOTF-MD to study the diffusion behavior of 19 protective coating candidates with intrinsic vacancies. In the defective structures of LiF, $LiMgAlF_6$, $LiAlSiO_4$, $LiYbAlF_6$, $Li_4Be_3P_3ClO_{12}$, $Li_4Be_3P_3BrO_{12}$, and Li_2CaHfF_8 no lithium hopping was observed at 700 K for 4 ns. The calculated migration energies for the other 12 coating candidates are listed in Table 6 along with the simulated Li vacancy concentration. These materials may make suitable coating materials if sufficient vacancy concentrations can be introduced without sacrificing stability.

4. CONCLUSION

Our benchmark results indicate that LOTF-MD offers advantages over high-temperature AIMD in accuracy and cost-efficiency when predicting lithium-ion migration energies. The mean absolute error in the calculated migration energies compared to experimental activation energies was reduced from 0.32 eV using AIMD to 0.13 eV using LOTF-MD, with the LOTF-MD calculations requiring only about one third the computational cost of AIMD. The benefit gained in using LOTF-MD is especially significant with intermediate-rate ionic conductors, such as those that might be useful as coating materials in solid state batteries. The reduced prediction error can be mainly attributed to the improved statistics by extended simulation time and the prevention of high-temperature phase transformations by enabling molecular dynamics simulations at moderate temperatures.

Our screen of possible coating materials based on high lithium content, a high oxidation limit of the electrochemical stability window, low chemical reactivity with sulfide electrolytes and oxide cathodes, and low lithium-ion migration energies reveals $Li_3Sc_2(PO_4)_3$ and $Li_3B_7O_{12}$ as promising candidates. $Li_3B_7O_{12}$ is predicted to provide excellent interfacial stability and has not to our knowledge been experimentally investigated for lithium-ion conductivity. If high vacancy concentrations can be introduced without sacrificing stability, Li_3AlF_6, $Li_2B_3O_4F_3$, $CsLi_2Cl_3$, LiCl, Li_2BeF_4, Li_3PO_4, $LiYF_4$, and $Li_2B_6O_9F_2$, $LiMgPO_4$, $LiLuF_4$ may also have suitably high stability and lithium-ion conductivity.

Table 5. LOTF-MD calculated migration energies in structures containing vacancies compared with experimental activation energies for 8 benchmark materials

MP entry id	Composition	$E_m \pm$ stderr (eV)	Experimental E_a (eV)	E_a - E_m (eV)
mp-10499	$LiZr_2P_3O_{12}$	0.15 ± 0.02	0.59	0.44
mp-30249	Li_4GeS_4	0.32 ± 0.02	0.52	0.20
mp-4556	Li_2SO_4	0.41 ± 0.02	1.20	0.79
mp-4558	Li_4GeO_4	0.54 ± 0.08	0.82	0.28
mp-554577	$Li_4P_2O_7$	0.46 ± 0.04	0.95	0.49
mp-641703	$Li_7P_3S_{11}$	0.20 ± 0.01	0.18	-0.02
mp-675083	Li_2MnCl_4	0.28 ± 0.03	0.63	0.35
mp-985583	β-Li_3PS_4	0.19 ± 0.01	0.16	-0.03

Table 6. LOTF-MD simulated Li migration energies and room-temperature ionic conductivities of candidate coating materials with introduced vacancies

MP entry id	Composition	Li vacancy concentration	LOTF-MD E_m (eV)	σ (300K) (S/cm)
mp-1185319	$LiCl$	6.25%	0.31 ± 0.02	9.53×10^{-4}
mp-1190687	$CsLi_2Cl_3$	6.25%	0.29 ± 0.14	3.26×10^{-6}
mp-1196457	$Li_2B_3O_4F_3$	6.25%	0.21 ± 0.03	4.67×10^{-4}
mp-1200209	$Li_2B_6O_9F_2$	8.33%	0.47 ± 0.05	6.59×10^{-6}
mp-13725	Li_3PO_4	4.17%	0.38 ± 0.06	1.97×10^{-5}
mp-15254	Li_3AlF_6	1.85%	0.24 ± 0.02	9.70×10^{-4}
mp-16828	$Li_3B_7O_{12}$	8.33%	0.51 ± 0.13	2.38×10^{-7}
mp-3700	$LiYF_4$	10.00%	0.39 ± 0.21	5.51×10^{-7}
mp-4622	Li_2BeF_4	4.17%	0.37 ± 0.04	5.41×10^{-5}
mp-561430	$LiLuF_4$	10.00%	0.62 ± 0.13	4.03×10^{-8}
mp-6565	$Li_3Sc_2(PO_4)_3$	4.17%	0.20 ± 0.02	4.47×10^{-3}
mp-9625	$LiMgPO_4$	6.25%	0.60 ± 0.10	4.40×10^{-8}

ASSOCIATED CONTENT

Supporting Information

Table of the computational parameters for the AIMD simulations; Table of combinations of coating materials, cathode materials, and electrolytes that form stable interfaces; Estimation of the upper limit of room temperature diffusivity in the materials screened out by the first filter at 700 K and the lower limit of diffusivity that can be evaluated within 200 ns. Discussion of the weighted least square regression of the Arrhenius equation and error analysis. (PDF)

AUTHOR INFORMATION

Corresponding Author.

*Tim Mueller E-mail: tmueller@jhu.edu

Notes
The authors declare no competing financial interest.

ACKNOWLEDGMENT

REFERENCES

1. Nishi, Y., Lithium ion secondary batteries; past 10 years and the future. *J Power Sources* **2001,** 100, (1-2), 101-106.
2. Janek, J.; Zeier, W. G., A solid future for battery development. *Nat Energy* **2016,** 1.
3. Wu, B. B.; Wang, S. Y.; Evans, W. J.; Deng, D. Z.; Yang, J. H.; Xiao, J., Interfacial behaviours between lithium ion conductors and electrode materials in various battery systems. *J Mater Chem A* **2016,** 4, (40), 15266-15280.
4. Bachman, J. C.; Muy, S.; Grimaud, A.; Chang, H. H.; Pour, N.; Lux, S. F.; Paschos, O.; Maglia, F.; Lupart, S.; Lamp, P.; Giordano, L.; Shao-Horn, Y., Inorganic Solid-State Electrolytes for Lithium Batteries: Mechanisms and Properties Governing Ion Conduction. *Chem Rev* **2016,** 116, (1), 140-62.
5. Takada, K.; Ohta, N.; Tateyama, Y., Recent Progress in Interfacial Nanoarchitectonics in Solid-State Batteries. *J Inorg Organomet P* **2015,** 25, (2), 205-213.
6. Luntz, A. C.; Voss, J.; Reuter, K., Interfacial Challenges in Solid-State Li Ion Batteries. *J Phys Chem Lett* **2015,** 6, (22), 4599-4604.
7. Li, Y. T.; Zhou, W. D.; Chen, X.; Lu, X. J.; Cui, Z. M.; Xin, S.; Xue, L. G.; Jia, Q. X.; Goodenough, J. B., Mastering the interface for advanced all-solid-state lithium rechargeable batteries. *P Natl Acad Sci USA* **2016,** 113, (47), 13313-13317.
8. Kim, J. G.; Son, B.; Mukherjee, S.; Schuppert, N.; Bates, A.; Kwon, O.; Choi, M. J.; Chung, H. Y.; Park, S., A review of lithium and non-lithium based solid state batteries. *J Power Sources* **2015,** 282, 299-322.
9. Jung, Y. S.; Oh, D. Y.; Nam, Y. J.; Park, K. H., Issues and Challenges for Bulk-Type All-Solid-State Rechargeable Lithium Batteries using Sulfide Solid Electrolytes. *Isr J Chem* **2015,** 55, (5), 472-485.
10. de Klerk, N. J. J.; Wagemaker, M., Space-Charge Layers in All-Solid-State Batteries; Important or Negligible? *ACS Appl Energ Mater* **2018,** 1, (10), 5609-5618.
11. Kerman, K.; Luntz, A.; Viswanathan, V.; Chiang, Y. M.; Chen, Z. B., Review-Practical Challenges Hindering the Development of Solid State Li Ion Batteries. *Journal of the Electrochemical Society* **2017,** 164, (7), A1731-A1744.
12. Zhu, Y. Z.; He, X. F.; Mo, Y. F., Origin of Outstanding Stability in the Lithium Solid Electrolyte Materials: Insights from Thermodynamic Analyses Based on First-Principles Calculations. *Acs Appl Mater Inter* **2015,** 7, (42), 23685-23693.
13. Auvergniot, J.; Cassel, A.; Ledeuil, J. B.; Viallet, V.; Seznec, V.; Dedryvere, R., Interface Stability of Argyrodite Li6PS5Cl toward LiCoO2, LiNi1/3Co1/3Mn1/3O2, and LiMn2O4 in Bulk All-Solid-State Batteries. *Chemistry of Materials* **2017,** 29, (9), 3883-3890.
14. Tian, Y. S.; Shi, T.; Richards, W. D.; Li, J. C.; Kim, J. C.; Bo, S. H.; Ceder, G., Compatibility issues between electrodes and electrolytes in solid-state batteries. *Energy & Environmental Science* **2017,** 10, (5), 1150-1166.
15. Zhu, Y. Z.; He, X. F.; Mo, Y. F., First principles study on electrochemical and chemical stability of solid electrolyte-electrode interfaces in all-solid-state Li-ion batteries. *J Mater Chem A* **2016,** 4, (9), 3253-3266.
16. Yubuchi, S.; Ito, Y.; Matsuyama, T.; Hayashi, A.; Tatsumisago, M., 5 V class LiNi0.5Mn1.5O4 positive electrode coated with Li3PO4 thin film for all-solid-state batteries using sulfide solid electrolyte. *Solid State Ionics* **2016,** 285, 79-82.

17.   Visbal, H.; Aihara, Y.; Ito, S.; Watanabe, T.; Park, Y.; Doo, S., The effect of diamond-like carbon coating on LiNi0.8Co0.15Al0.05O2 particles for all solid-state lithium-ion batteries based on Li2S-P2S5 glass-ceramics. *J Power Sources* **2016,** 314, 85-92.

18.   Seino, Y.; Ota, T.; Takada, K., High rate capabilities of all-solid-state lithium secondary batteries using Li4Ti5O12-coated LiNi0.8Co0.15Al0.05O2 and a sulfide-based solid electrolyte. *J Power Sources* **2011,** 196, (15), 6488-6492.

19.   Machida, N.; Kashiwagi, J.; Naito, M.; Shigematsu, T., Electrochemical properties of all-solid-state batteries with ZrO2-coated LiNi1/3Mn1/3Co1/3O2 as cathode materials. *Solid State Ionics* **2012,** 225, 354-358.

20.   Kim, J.; Kim, M.; Noh, S.; Lee, G.; Shin, D., Enhanced electrochemical performance of surface modified LiCoO2 for all-solid-state lithium batteries. *Ceram Int* **2016,** 42, (2), 2140-2146.

21.   Kato, Y.; Hori, S.; Saito, T.; Suzuki, K.; Hirayama, M.; Mitsui, A.; Yonemura, M.; Iba, H.; Kanno, R., High-power all-solid-state batteries using sulfide superionic conductors. *Nat Energy* **2016,** 1.

22.   Ito, S.; Fujiki, S.; Yamada, T.; Aihara, Y.; Park, Y.; Kim, T. Y.; Baek, S. W.; Lee, J. M.; Doo, S.; Machida, N., A rocking chair type all-solid-state lithium ion battery adopting Li2O-ZrO2 coated LiNi0.8Co0.15Al0.05O2 and a sulfide based electrolyte. *J Power Sources* **2014,** 248, 943-950.

23.   Aihara, Y.; Ito, S.; Omoda, R.; Yamada, T.; Fujiki, S.; Watanabe, T.; Park, Y.; Doo, S., The Electrochemical Characteristics and Applicability of an Amorphous Sulfide-Based Solid Ion Conductor for the Next-Generation Solid-State Lithium Secondary Batteries. *Front Energy Res* **2016,** 4.

24.   Li, X.; Jin, L.; Song, D.; Zhang, H.; Shi, X.; Wang, Z.; Zhang, L.; Zhu, L., LiNbO3-coated LiNi0.8Co0.1Mn0.1O2 cathode with high discharge capacity and rate performance for all-solid-state lithium battery. *Journal of Energy Chemistry* **2020,** 40, 39-45.

25.   Ohta, N.; Takada, K.; Sakaguchi, I.; Zhang, L.; Ma, R.; Fukuda, K.; Osada, M.; Sasaki, T., LiNbO3-coated LiCoO2 as cathode material for all solid-state lithium secondary batteries. *Electrochem Commun* **2007,** 9, (7), 1486-1490.

26.   Sakuda, A.; Kitaura, H.; Hayashi, A.; Tadanaga, K.; Tatsumisago, M., All-solid-state lithium secondary batteries with oxide-coated LiCoO2 electrode and Li2S–P2S5 electrolyte. *J Power Sources* **2009,** 189, (1), 527-530.

27.   Ito, S.; Fujiki, S.; Yamada, T.; Aihara, Y.; Park, Y.; Kim, T. Y.; Baek, S.-W.; Lee, J.-M.; Doo, S.; Machida, N., A rocking chair type all-solid-state lithium ion battery adopting Li2O–ZrO2 coated LiNi0.8Co0.15Al0.05O2 and a sulfide based electrolyte. *J Power Sources* **2014,** 248, 943-950.

28.   Takada, K.; Ohta, N.; Zhang, L.; Fukuda, K.; Sakaguchi, I.; Ma, R.; Osada, M.; Sasaki, T., Interfacial modification for high-power solid-state lithium batteries. *Solid State Ionics* **2008,** 179, (27-32), 1333-1337.

29.   Ohta, S.; Komagata, S.; Seki, J.; Saeki, T.; Morishita, S.; Asaoka, T., All-solid-state lithium ion battery using garnet-type oxide and Li3BO3 solid electrolytes fabricated by screen-printing. *J Power Sources* **2013,** 238, 53-56.

30.   Han, F.; Yue, J.; Chen, C.; Zhao, N.; Fan, X.; Ma, Z.; Gao, T.; Wang, F.; Guo, X.; Wang, C., Interphase Engineering Enabled All-Ceramic Lithium Battery. *Joule* **2018,** 2, (3), 497-508.

31.   Aykol, M.; Kim, S.; Hegde, V. I.; Snydacker, D.; Lu, Z.; Hao, S. Q.; Kirklin, S.; Morgan, D.; Wolverton, C., High-throughput computational design of cathode coatings for Li-ion batteries. *Nat Commun* **2016,** 7.

32.   Jain, A.; Hautier, G.; Ong, S. P.; Moore, C.; Kang, B.; Chen, H. L.; Ma, X. H.; Kim, J. C.; Kocher, M.; Gunter, D.; Cholia, S.; Greiner, A.; Bailey, D. H.; Skinner, D.; Persson, K.; Ceder, G., Materials Project: A public materials database and its application to lithium ion battery cathode design. *Abstr Pap Am Chem S* **2012,** 243.

33.   Saal, J. E.; Kirklin, S.; Aykol, M.; Meredig, B.; Wolverton, C., Materials Design and Discovery with High-Throughput Density Functional Theory: The Open Quantum Materials Database (OQMD). *Jom-Us* **2013,** 65, (11), 1501-1509.

34.   Snydacker, D. H.; Hegde, V. I.; Wolverton, C., Electrochemically Stable Coating Materials for Li, Na, and Mg Metal Anodes in Durable High Energy Batteries. *Journal of the Electrochemical Society* **2017,** 164, (14), A3582-A3589.

35.   Xiao, Y.; Miara, L. J.; Wang, Y.; Ceder, G., Computational Screening of Cathode Coatings for Solid-State Batteries. *Joule* **2019,** 3, (5), 1252-1275.

36.   Zhang, Z.; Shao, Y.; Lotsch, B.; Hu, Y.-S.; Li, H.; Janek, J.; Nazar, L. F.; Nan, C.-W.; Maier, J.; Armand, M.; Chen, L., New horizons for inorganic solid state ion conductors. *Energy & Environmental Science* **2018,** 11, (8), 1945-1976.

37.   Cao, C.; Li, Z.-B.; Wang, X.-L.; Zhao, X.-B.; Han, W.-Q., Recent Advances in Inorganic Solid Electrolytes for Lithium Batteries. *Front Energy Res* **2014,** 2.

38.   Oh, G.; Hirayama, M.; Kwon, O.; Suzuki, K.; Kanno, R., Bulk-Type All Solid-State Batteries with 5 V Class LiNi0.5Mn1.5O4 Cathode and Li10GeP2S12 Solid Electrolyte. *Chemistry of Materials* **2016,** 28, (8), 2634-2640.

39.   Li, X.; Liu, J.; Banis, M. N.; Lushington, A.; Li, R.; Cai, M.; Sun, X., Atomic layer deposition of solid-state electrolyte coated cathode materials with superior high-voltage cycling behavior for lithium ion battery application. *Energy Environ. Sci.* **2014,** 7, (2), 768-778.

40.   Henkelman, G.; Uberuaga, B. P.; Jonsson, H., A climbing image nudged elastic band method for finding saddle points and minimum energy paths. *Journal of Chemical Physics* **2000,** 113, (22), 9901-9904.

41.   Henkelman, G.; Jonsson, H., Improved tangent estimate in the nudged elastic band method for finding minimum energy paths and saddle points. *Journal of Chemical Physics* **2000,** 113, (22), 9978-9985.

42.   Muy, S.; Bachman, J. C.; Giordano, L.; Chang, H. H.; Abernathy, D. L.; Bansal, D.; Delaire, O.; Hori, S.; Kanno, R.; Maglia, F.; Lupart, S.; Lamp, P.; Shao-Horn, Y., Tuning mobility and stability of lithium ion conductors based on lattice dynamics. *Energy & Environmental Science* **2018,** 11, (4), 850-859.

43.   Brown, I. D., Recent developments in the methods and applications of the bond valence model. *Chem Rev* **2009,** 109, (12), 6858-919.

44.   He, X. F.; Zhu, Y. Z.; Epstein, A.; Mo, Y. F., Statistical variances of diffusional properties from ab initio molecular dynamics simulations. *Npj Computational Materials* **2018,** 4.

45.   Shapeev, A. V., Moment Tensor Potentials: A Class of Systematically Improvable Interatomic Potentials. *Multiscale Modeling & Simulation* **2016,** 14, (3), 1153-1173.

46.   Manzhos, S.; Dawes, R.; Carrington, T., Neural network-based approaches for building high dimensional and quantum dynamics-friendly potential energy surfaces. *International Journal of Quantum Chemistry* **2015,** 115, (16), 1012-1020.

47.   Kondati Natarajan, S.; Morawietz, T.; Behler, J., Representing the potential-energy surface of protonated water clusters by high-dimensional neural network potentials. *Phys Chem Chem Phys* **2015,** 17, (13), 8356-71.

48.   Behler, J., Representing potential energy surfaces by high-dimensional neural network potentials. *J Phys Condens Matter* **2014,** 26, (18), 183001.

49.   Behler, J., Neural network potential-energy surfaces in chemistry: a tool for large-scale simulations. *Phys Chem Chem Phys* **2011,** 13, (40), 17930-55.

50.   Bartok, A. P.; Payne, M. C.; Kondor, R.; Csanyi, G., Gaussian approximation potentials: the accuracy of quantum mechanics, without the electrons. *Phys Rev Lett* **2010,** 104, (13), 136403.

51.   Li, Z.; Kermode, J. R.; De Vita, A., Molecular dynamics with on-the-fly machine learning of quantum-mechanical forces. *Phys Rev Lett* **2015,** 114, (9), 096405.

52.   Botu, V.; Ramprasad, R., Adaptive machine learning framework to accelerate ab initio molecular dynamics. *International Journal of Quantum Chemistry* **2015,** 115, (16), 1074-1083.

53.   Perdew, J. P.; Emzerhof, M.; Burke, K., Rationale for mixing exact exchange with density functional approximations. *Journal of Chemical Physics* **1996,** 105, (22), 9982-9985.

54.   Blochl, P. E., Projector Augmented-Wave Method. *Physical Review B* **1994,** 50, (24), 17953-17979.

55.   Ong, S. P.; Mo, Y. F.; Richards, W. D.; Miara, L.; Lee, H. S.; Ceder, G., Phase stability, electrochemical stability and ionic conductivity of the Li10 +/- 1MP2X12 (M = Ge, Si, Sn, Al or P, and X = O, S or Se) family of superionic conductors. *Energy & Environmental Science* **2013,** 6, (1), 148-156.

56.   Zhu, Z. Y.; Chu, I. H.; Ong, S. P., Li3Y(PS4)(2) and Li5PS4Cl2: New Lithium Superionic Conductors Predicted from Silver Thiophosphates using Efficiently Tiered Ab Initio Molecular Dynamics Simulations. *Chemistry of Materials* **2017,** 29, (6), 2474-2484.

57.   Gubaev, K.; Podryabinkin, E. V.; Hart, G. L. W.; Shapeev, A. V., Accelerating high-throughput searches for new alloys with active learning of interatomic potentials. *Comp Mater Sci* **2019,** 156, 148-156.

58.   Plimpton, S., Fast Parallel Algorithms for Short-Range Molecular Dynamics. *J. Comput. Phys.* **1995,** 117, (1), 1-19.

59.   Podryabinkin, E. V.; Shapeev, A. V., Active learning of linearly parametrized interatomic potentials. *Comp Mater Sci* **2017,** 140, 171-180.

60.   Settles, B., Active Learning Literature Survey.

61.   Novoselov, I. I.; Yanilkin, A. V.; Shapeev, A. V.; Podryabinkin, E. V., Moment tensor potentials as a promising tool to study diffusion processes. *Comp Mater Sci* **2019,** 164, 46-56.

62.   Marcolongo, A.; Marzari, N., Ionic correlations and failure of Nernst-Einstein relation in solid-state electrolytes. *Physical Review Materials* **2017,** 1, (2).

63.   de Klerk, N. J. J.; van der Maas, E.; Wagemaker, M., Analysis of Diffusion in Solid-State Electrolytes through MD Simulations, Improvement of the Li-Ion Conductivity in beta-Li3PS4 as an Example. *ACS Appl Energy Mater* **2018,** 1, (7), 3230-3242.

64.   Hori, S.; Kato, M.; Suzuki, K.; Hirayama, M.; Kato, Y.; Kanno, R.; Sprenkle, V., Phase Diagram of the Li4GeS4-Li3PS4 Quasi-Binary System Containing the Superionic Conductor Li10GeP2S12. *Journal of the American Ceramic Society* **2015,** 98, (10), 3352-3360.

65.   Kumar, M.; Yadav, A. K.; Anita; Sen, S.; Kumar, S., Lithium Ion Conduction In Sol-Gel Synthesized LiZr2(PO4)(3) Polymorphs. *62nd Dae Solid State Physics Symposium* **2018,** 1942.

66.   Kumar, S.; Balaya, P., Improved ionic conductivity in NASICON-type Sr 2+ doped LiZr 2 (PO 4) 3. *Solid State Ionics* **2016,** 296, 1-6.

67.   Kanno, R., Synthesis of a new lithium ionic conductor, thio-LISICON–lithium germanium sulfide system. *Solid State Ionics* **2000,** 130, (1-2), 97-104.

68.   Wijayasekera, C.; Mellander, B., Phase transitions and ionic conductivity of the lithium sulphate-lithium phosphate system. *Solid State Ionics* **1991,** 45, (3-4), 293-298.

69.   Rama Rao, S.; Bheema Lingam, C.; Rajesh, D.; Vijayalakshmi, R. P.; Sunandana, C. S., Structural, conductivity and dielectric properties of Li2SO4. *The European Physical Journal Applied Physics* **2014,** 66, (3).

70.   Liebert, B. E.; Huggins, R. A., Ionic conductivity of Li4GeO4, Li2GeO3 and Li2Ge7O15. *Mater Res Bull* **1976,** 11, (5), 533-538.

71.   Hodge, I. M.; Ingram, M. D.; West, A. R., Ionic Conductivity of Li4SiO, Li4GeO4, and Their Solid Solutions. *Journal of the American Ceramic Society* **1976,** 59, (7-8), 360-366.

72.   Zaafouri, A.; Megdiche, M.; Gargouri, M., Studies of electric, dielectric, and conduction mechanism by OLPT model of Li4P2O7. *Ionics* **2015,** 21, (7), 1867-1879.

73.   Chu, I. H.; Nguyen, H.; Hy, S.; Lin, Y. C.; Wang, Z.; Xu, Z.; Deng, Z.; Meng, Y. S.; Ong, S. P., Insights into the Performance Limits of the Li7P3S11 Superionic Conductor: A Combined First-Principles and Experimental Study. *ACS Appl Mater Interfaces* **2016,** 8, (12), 7843-53.

74.   Homma, K.; Yonemura, M.; Kobayashi, T.; Nagao, M.; Hirayama, M.; Kanno, R., Crystal structure and phase transitions of the lithium ionic conductor Li3PS4. *Solid State Ionics* **2011,** 182, (1), 53-58.

75.   Whittingham, M. S., Lithium Batteries and Cathode Materials. *Chemical Reviews* **2004,** 104, (10), 4271-4302.

76.   Lin, L. D.; Liang, F.; Zhang, K. Y.; Mao, H. Z.; Yang, J.; Qian, Y. T., Lithium phosphide/lithium chloride coating on lithium for advanced lithium metal anode. *J Mater Chem A* **2018,** 6, (32), 15859-15867.

77.   Courtcastagnet, R.; Kaps, C.; Cros, C.; Hagenmuller, P., Ionic Conductivity-Enhancement of Licl by Homogeneous and Heterogeneous Dopings. *Solid State Ionics* **1993,** 61, (4), 327-334.

78.   Bykov, A., Superionic conductors Li3M2(PO4)3 (M═Fe, Sc, Cr): Synthesis, structure and electrophysical properties. *Solid State Ionics* **1990,** 38, (1-2), 31-52.

79.   Zhao, X.; Zhang, Z.; Zhang, X.; Tang, B.; Xie, Z.; Zhou, Z., Computational screening and first-principles investigations of NASICON-type LixM2(PO4)3 as solid electrolytes for Li batteries. *J Mater Chem A* **2018,** 6, (6), 2625-2631.

80.   Islam, M. M.; Bredow, T.; Heitjans, P., The ionic conductivity in lithium-boron oxide materials and its relation to structural, electronic and defect properties: insights from theory. *J Phys Condens Matter* **2012,** 24, (20), 203201.

81.   Pilz, T.; Jansen, M., Li2B6O9F2, a New Acentric Fluorooxoborate. *Zeitschrift Fur Anorganische Und Allgemeine Chemie* **2011,** 637, (14-15), 2148-2152.

82.   Muy, S.; Bachman, J. C.; Giordano, L.; Chang, H.-H.; Abernathy, D. L.; Bansal, D.; Delaire, O.; Hori, S.; Kanno, R.; Maglia, F.; Lupart, S.; Lamp, P.; Shao-Horn, Y., Tuning mobility and stability of lithium ion conductors based on lattice dynamics. *Energy & Environmental Science* **2018,** 11, (4), 850-859.

83.   Vashman, A. A.; Pronin, I. S.; Sigaryov, S. E., Superionic Compound Li3sc2(Po4)3 - Nmr-Spectra and Nuclear Magnetic-Relaxation. *Solid State Ionics* **1992,** 58, (3-4), 201-215.

84.   Pilz, T.; Nuss, H.; Jansen, M., Li2B3O4F3, a new lithium-rich fluorooxoborate. *J Solid State Chem* **2012,** 186, 104-108.

Electronic Supplementary Information for "Lithium ion conduction in cathode coating materials from on-the-fly machine learning"

Chuhong Wang, Koutarou Aoyagi, Pandu Wisesa, Tim Mueller[*]

Table S1: Computational parameters of AIMD simulations

	MP entry id	Composition	Number of atoms in simulated supercell	VASP PAW-PBE potentials
Experimental benchmark	mp-10499	$LiZr_2(PO_4)_3$	144	Li_sv, Zr_sv, P, O
	mp-30249	Li_4GeS_4	72	Li_sv, Ge_d, S
	mp-4556	Li_2SO_4	56	Li_sv, S, O
	mp-4558	Li_4GeO_4	72	Li_sv, Ge_d, O
	mp-554577	$Li_4P_2O_7$	104	Li_sv, P, O
	mp-641703	$Li_7P_3S_{11}$	84	Li_sv, P, S
	mp-675083	Li_2MnCl_4	56	Li_sv, Mn_pv, Cl
	mp-985583	Li_3PS_4	64	Li_sv, P, S
Interface protective coating candidates	mp-10103	$LiYbAlF_6$	72	Li_sv, Yb_2, Al, F
	mp-1138	LiF	72	Li_sv, F
	mp-1185319	LiCl	32	Li_sv, Cl
	mp-1190687	$CsLi_2Cl_3$	48	Cs_sv_GW, Li_sv, Cl
	mp-1193222	$LiMgAlF_6$	81	Li_sv, Mg_pv, Al, F
	mp-1196457	$Li_2B_3O_4F_3$	96	Li_sv, B, O, F
	mp-1200209	$Li_2B_6O_9F_2$	114	Li_sv, B, O, F
	mp-13725	Li_3PO_4	64	Li_sv, P, O
	mp-15254	Li_3AlF_6	180	Li_sv, Al, F
	mp-16577	Li_2CaHfF_8	60	Li_sv, Ca_sv, Hf_pv, F
	mp-16828	$Li_3B_7O_{12}$	88	Li_sv, B, O
	mp-18220	$LiAlSiO_4$	84	Li_sv, Al, Si, O
	mp-3700	$LiYF_4$	60	Li_sv, Y_sv, F
	mp-4622	Li_2BeF_4	84	Li_sv, Be_sv, F
	mp-554560	$Li_4Be_3P_3BrO_{12}$	92	Li_sv, Be_sv, P, Br, O

	mp-560894	$Li_4Be_3P_3ClO_{12}$	92	Li_sv, Be_sv, P, Cl, O
	mp-561430	$LiLuF_4$	60	Li_sv, Lu_3, F
	mp-6565	$Li_3Sc_2(PO_4)_3$	160	Li_sv, Sc_sv, P, O
	mp-9625	$LiMgPO_4$	112	Li_sv, Mg_pv, P, O

Table S2: 19 protective coating material candidates and compatible battery components correspondingly

MP entry id	Composition	Cathode	Sulfide - based solid electrolyte
mp-10103	$LiYbAlF_6$	$Li(MnNiCo)_{1/3}O_2$ $Li_2Mn_3NiO_8$ $LiFePO_4$	$Li_{10}GeP_2S_{12}$ $Li_{10}SiP_2S_{12}$ $Li_{10}SnP_2S_{12}$ $Li_7P_3S_{11}$
mp-1138	LiF	$Li(MnNiCo)_{1/3}O_2$ $LiCoO_2$ $LiFePO_4$ $LiMn_2O_4$	$Li_{10}GeP_2S_{12}$ $Li_{10}SiP_2S_{12}$ $Li_{10}SnP_2S_{12}$ Li_6PS_5Br Li_6PS_5Cl $Li_7P_3S_{11}$
mp-1185319	$LiCl$	$Li(MnNiCo)_{1/3}O_2$ $LiCoO_2$ $LiMn_2O_4$ $LiFePO_4$	$Li_{10}GeP_2S_{12}$ $Li_{10}SiP_2S_{12}$ $Li_{10}SnP_2S_{12}$ Li_6PS_5Br Li_6PS_5Cl $Li_7P_3S_{11}$
mp-1190687	$CsLi_2Cl_3$	$Li(MnNiCo)_{1/3}O_2$	$Li_{10}GeP_2S_{12}$ $Li_{10}SnP_2S_{12}$ Li_6PS_5Cl
mp-1193222	$LiMgAlF_6$	$Li(MnNiCo)_{1/3}O_2$ $Li_2Mn_3NiO_8$ $LiFePO_4$	$Li_7P_3S_{11}$
mp-1196457	$Li_2B_3O_4F_3$	$Li(MnNiCo)_{1/3}O_2$ $LiFePO_4$	$Li_7P_3S_{11}$
mp-1200209	$Li_2B_6O_9F_2$	$Li(MnNiCo)_{1/3}O_2$ $Li_2Mn_3NiO_8$ $LiFePO_4$	$Li_7P_3S_{11}$
mp-13725	Li_3PO_4	$Li(MnNiCo)_{1/3}O_2$ $LiCoO_2$ $LiMn_2O_4$	$Li_{10}GeP_2S_{12}$ $Li_{10}SnP_2S_{12}$ Li_6PS_5Br Li_6PS_5Cl $Li_7P_3S_{11}$

mp-15254	Li_3AlF_6	$Li(MnNiCo)_{1/3}O_2$ $Li_2Mn_3NiO_8$ $LiFePO_4$	$Li_{10}GeP_2S_{12}$ $Li_{10}SnP_2S_{12}$ $Li_7P_3S_{11}$
mp-16577	Li_2CaHfF_8	$Li(MnNiCo)_{1/3}O_2$ $Li_2Mn_3NiO_8$ $LiFePO_4$	$Li_7P_3S_{11}$
mp-16828	$Li_3B_7O_{12}$	$Li(MnNiCo)_{1/3}O_2$ $LiCoO_2$ $LiFePO_4$	$Li_{10}GeP_2S_{12}$ $Li_{10}SiP_2S_{12}$ $Li_{10}SnP_2S_{12}$ Li_6PS_5Br Li_6PS_5Cl $Li_7P_3S_{11}$
mp-18220	$LiAlSiO_4$	$Li(MnNiCo)_{1/3}O_2$ $LiCoO_2$	$Li_{10}GeP_2S_{12}$ $Li_{10}SiP_2S_{12}$ $Li_{10}SnP_2S_{12}$ Li_6PS_5Br
mp-3700	$LiYF_4$	$Li(MnNiCo)_{1/3}O_2$ $Li_2Mn_3NiO_8$ $LiFePO_4$	$Li_{10}GeP_2S_{12}$ $Li_7P_3S_{11}$
mp-4622	Li_2BeF_4	$Li(MnNiCo)_{1/3}O_2$ $Li_2Mn_3NiO_8$ $LiFePO_4$	$Li_{10}GeP_2S_{12}$ $Li_{10}SiP_2S_{12}$ $Li_{10}SnP_2S_{12}$ Li_6PS_5Br Li_6PS_5Cl $Li_7P_3S_{11}$
mp-554560	$Li_4Be_3P_3BrO_{12}$	$Li(MnNiCo)_{1/3}O_2$ $LiFePO_4$	$Li_{10}GeP_2S_{12}$ $Li_{10}SnP_2S_{12}$ Li_6PS_5Br Li_6PS_5Cl $Li_7P_3S_{11}$
mp-560894	$Li_4Be_3P_3ClO_{12}$	$Li(MnNiCo)_{1/3}O_2$ $LiFePO_4$	$Li_{10}GeP_2S_{12}$ $Li_{10}SnP_2S_{12}$ Li_6PS_5Cl $Li_7P_3S_{11}$

mp-561430	$LiLuF_4$	$Li(MnNiCo)_{1/3}O_2$ $Li_2Mn_3NiO_8$ $LiFePO_4$	$Li_{10}GeP_2S_{12}$ $Li_{10}SiP_2S_{12}$ $Li_{10}SnP_2S_{12}$ Li_6PS_5Br Li_6PS_5Cl $Li_7P_3S_{11}$
mp-6565	$Li_3Sc_2(PO_4)_3$	$Li(MnNiCo)_{1/3}O_2$ $LiFePO_4$	$Li_7P_3S_{11}$
mp-9625	$LiMgPO_4$	$Li(MnNiCo)_{1/3}O_2$ $LiFePO_4$	$Li_7P_3S_{11}$

S3: Lowest diffusivity with a relative standard deviation of at least 0.5 observable in 200 nanoseconds

He, X. F., et al. defined the relative standard deviation as the ratio between the standard deviation of the diffusivity and the diffusivity itself.[1] Through a series of benchmarks they fit the following equation for the relative standard deviation (RSD) of lithium-ion diffusivities:

$$RSD = \frac{\sigma_D}{D_{true}} = \frac{3.43}{\sqrt{N_{eff}}} + 0.04 \tag{1}$$

where

$$N_{eff} = \frac{\max_{\Delta t}\left[\text{TMSD}(\Delta t)\right]}{a^2} \tag{2}$$

where $\text{TMSD}(\Delta t)$ is the total mean squared displacement (the sum of the mean squared displacements of the lithium atoms) after time Δt and a is the length of a lithium ion hop.

$$\text{TMSD}(\Delta t) = \frac{\text{MSD}(\Delta t)}{N} \tag{3}$$

where N is the total number of mobile ions in the simulated supercell. We use 3 Å as the estimate for a. Based on the above equations, $\text{TMSD}(\Delta t)$ must reach at least 500 Å² to achieve $RSD \leq 0.5$. The diffusivity is calculated as the slope between MSD among all mobile ions and the time interval according to Einstein relation:

$$D = \frac{\text{MSD}(\Delta t)}{6\Delta t} \tag{4}$$

Following equations (1) and (4) with the assumption of 20 lithium atoms per supercell and the longest simulation time of 200 nanoseconds, we estimate $2 \times 10^{-9}\,\text{cm}^2/\text{sec}$ to be the lowest diffusivity we can calculate with the constraint of $RSD \leq 0.5$.

S4: Estimation of room temperature diffusivity

If no diffusive hops have been observed in the first 4 nanoseconds, we estimate the upper limit of diffusivity by assuming that each Li^+ undergoes a site-to-site hopping exactly every 4 nanoseconds. The materials in this study have a typical hopping distance between adjacent Li sites of about 3 Å. Using equation (4) we estimate the upper limit on Li diffusivity at 700K $D = \frac{1}{6} \times \frac{(3 \text{ Å})^2}{4 \text{ } ns} = 3.75 \times 10^{-8} \text{cm}^2/\text{sec}$. Suppose the material has an intermediate activation barrier of 0.5 eV, we extrapolate the diffusivity at 700K down to 300K assuming Arrhenius scaling by a factor of $\frac{D(300K)}{D(700K)} = \frac{e^{-\frac{0.5}{300k}}}{e^{-\frac{0.5}{700k}}} = 1.6 \times 10^{-5}$, which gives room-temperature diffusivity of $6 \times 10^{-13} \text{cm}^2/\text{sec}$.

S5: Arrhenius fitting and error analysis

To estimate the uncertainty in the calculated activation energies we start from the Arrhenius equation

$$D(T) = D_0 e^{-\frac{E_a}{k_B T}} \tag{5}$$

where $D(T)$ is the diffusivity at temperature T, D_0 is the diffusivity in the limit of infinite temperature, and E_a is the activation energy for diffusion. Taking the natural log of both sides gives an equation that is linear in E_a:

$$\ln(D(T)) = \ln(D_0) - \frac{E_a}{k_B T} \tag{6}$$

The variance of $\ln(D(T))$, $\sigma^2_{\ln(D(T))}$, is approximately related to the variance in $D(T)$, $\sigma^2_{D_T}$, through the following equation:[2]

$$\sigma^2_{\ln(D(T))} \approx \frac{\sigma^2_{D_T}}{D_T^2} \tag{7}$$

where we estimate $\sigma^2_{D_T}$ using the equation of He, X. F., et al.[1] (Equation(2)). We estimate E_a by performing a weighted least squares regression[3] of $\ln(D(T))$ with respect to $\frac{1}{k_B T}$, where the weight of each sample is the inverse of $\sigma^2_{\ln(D(T))}$ for that sample. E_a is a coefficient of the linear estimator, and the variance of E_a is taken as the square of the standard error of the coefficient. The weighted least squares regression and standard error of the coefficient were calculated using the SciPy package. [4]

References Cited

1.   He, X. F.; Zhu, Y. Z.; Epstein, A.; Mo, Y. F., Statistical variances of diffusional properties from ab initio molecular dynamics simulations. *Npj Computational Materials* **2018,** 4.
2.   Liu, X., *Survival Analysis*. 2012.
3.   Pattengill, M. D.; Sands, D. E., Statistical Significance of Linear Least-Squares Parameters. *Journal of Chemical Education* **1979,** 56, (4), 244-247.
4.   Jones, E.; Oliphant, T.; Peterson, P.; others SciPy: Open Source Scientific Tools for Python. https://docs.scipy.org